Eur. Phys. J. D **38**, 129–138 (2006)
DOI: 10.1140/epjd/e2005-00284-4

THE EUROPEAN
PHYSICAL JOURNAL D

Effect of the molecular structure on the gas-surface scattering studied by supersonic molecular beam

T. Kondo[1,a], H.S. Kato[1], T. Yamada[1], S. Yamamoto[2], and M. Kawai[1,3,b]

[1] Surface Chemistry Laboratory, RIKEN (Institute of Chemical and Physical Research), 2-1 Hirosawa, Wako, Saitama 351-0198, Japan
[2] National Institute of Advanced Industrial Science and Technology (AIST) AIST Tsukuba Central 2, 1-1-1 Umezono, Tsukuba 305-8568, Japan
[3] Department of Advanced Materials Science, Graduate School of Frontier Sciences, University of Tokyo, Kashiwa, Chiba 277-8561, Japan

Received 20 July 2005 / Received in final form 20 September 2005

Abstract. The experimental apparatus for investigating the gas-surface interaction has been newly developed. The coherent length of the helium, the energy resolution and the angular spread of the beam in the apparatus were established as $\omega = 16$ nm, $\Delta E/E = 2.4\%$ and $\Delta\theta = 0.5°$, respectively, through the measurements of the time-of-flight of He beam and of the angular intensity distributions of He scattered from LiF(001). The angular intensity distributions of Ar, N_2 and CO scattered from the LiF(001) surface along the [100] azimuthal direction were then measured as a function of incident translational energy. The effects of the molecular structural anisotropy and center-of-mass position on the gas-surface inelastic collision at the corrugated surface are discussed with predictions based on a recently developed simple classical theory of the ellipsoid-washboard model.

PACS. 68.49.Bc Atom scattering from surfaces (diffraction and energy transfer) – 68.49.Df Molecule scattering from surfaces (energy transfer, resonances, trapping) – 34.50.Dy Interactions of atoms and molecules with surfaces; photon and electron emission; neutralization of ions – 68.49.-h Surface characterization by particle-surface scattering

1 Introduction

The gas-surface collision is the initial step of all of the chemical reactions on a surface. During collision processes, the kinetic energy of reactant gas molecules is dissipated into such channels as phonon creation and/or electronic excitation in solid, internal mode excitation of gas molecules, and so on. The energy dissipative inelastic collision process depends on the energy state of the incoming molecule, the surface temperature and the potential energy surface of the molecule interacting with the surface. As inelastic collision processes play important roles especially in the case of heavy gas molecules, their collision dynamics on a wide variety of well-defined single-crystal surfaces have been extensively investigated predominantly by the supersonic molecular beam scattering technique [1–6].

For the collision of a heavy rare gas atom with a surface, its energy dissipation process is qualitatively well described by a simple classical collision model such as the hard-cube model [7], despite its simplicity, where the process is described only by surface temperature, incident translational energy, incident angle and mass ratio between gas and surface. Even on the corrugated surface, the scattering processes such as rainbow scattering [8] have been qualitatively described with the concept of the cube model by introducing the structural surface corrugation in the model [9,10].

On the other hand, for a linear and/or polyatomic molecule, due to their internal modes, several inelastic collision processes take place such as chattering collision [11–15], rotational rainbow [8,16–19] and rotational trapping [18–22]. The precise semi-classical theory dealing with gas-surface collision for heavy polyatomic molecule is recently developed [23,24] and is successful in describing the scattering phenomena such as scattering of C_2H_2, CH_4 and O_2 from relatively flat surfaces [25–28]. We have also recently developed a simple classical theory of the ellipsoid-washboard model [29], which simplifies the inelastic collision of such complicated gas-surface scattering system.

In this article, we will report on the effects of the molecular structure on the gas-surface collision by precisely measuring the angular intensity distributions of He,

---

[a] e-mail: `takahiro@riken.jp`
[b] e-mail: `maki@riken.jp`

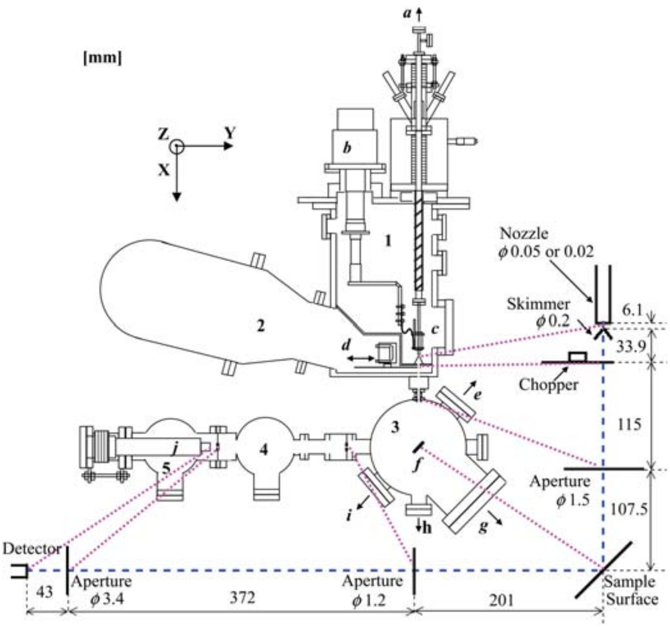

Fig. 1. Schematic diagram of experimental apparatus: (1) molecular beam source chamber; (2) chopper chamber; (3) scattering chamber; (4) time-of-flight chamber, and (5) detector chamber. Also, (a) He/Ne laser, (b) closed-cycle helium refrigerator, (c) heater, (d) chopper, (e) RAIRS detector, (f) sample, (g) LEED/AES, (h) port for detector units in time-of-flight measurement, (i) RAIRS source and (j) quadrupole mass spectrometer. The ion gun and oxygen source are slanted by 45° below the scattering plane facing the sample. The aperture diameters are also shown with distance along the beam.

Ar, CO and N_2 scattered from LiF(001) and by comparing the results with predictions based on the ellipsoid-washboard model [29]. Section 2 describes the newly developed experimental apparatus and method in detail, Section 3 gives the experimental results together with the analysis and discussion and Section 4 is our conclusion.

2 Experiment

2.1 Apparatus

The experimental apparatus used in this work is shown schematically in Figure 1. It was designed based on a similar apparatus which was previously reported in elsewhere [30,31]. There are mainly five major advantages in the new design; (1) narrow energy spread of the low energy He beam owing to the closed-cycle refrigerator attached to the beam nozzle; (2) wide range attainable surface temperature owing to the good thermal contact of the sample holder with the rod for liquid nitrogen; (3) enough space for the set-up of the reflection absorption infrared spectroscopy (RAIRS) system which enables us to measure the change of the surface condition simultaneously with the measurement of He atom scattering; (4) easy assemble system of the detector chamber with differential pumping stage for conducting the scattering experiment with different total scattering angle (incident plus scattering angles) and for the measurement of the time-of-flight spectra of the incident beam; (5) effective heating system of the gas-line [32] in the beam source for the beam of liquid molecule such as H_2O. Details of the apparatus are quantitatively described below.

The apparatus consists of five stainless-steel chambers: (1) molecular beam source chamber, (2) chopper chamber, (3) scattering chamber, (4) time-of-flight chamber, and (5) detector chamber. Each chamber is independently pumped to ultrahigh vacuum. The internal walls of chambers 3, 4 and 5 are polished by electrochemical buffering to achieve a base pressure of less than 10^{-10} Torr. Chambers 2, 3, and 4 are connected through bellow-nipples and gate valves for their alignment and maintenance. The translational and angular alignments of each chamber with respect to the molecular beam are established by individual adjustable mounts.

Chamber 1 consists of a beam source and a skimmer. It is evacuated by a diffusion pump with a pumping speed of 2000 l/s (for N_2). A supersonic molecular beam is generated by free-jet expansion from a pinhole of a cylindrical nozzle and skimmed by a conical skimmer into chamber 2. The diameter of the nozzle pinhole is set to 0.05 and 0.02 mm for the molecular beam source and He beam source, respectively. The nozzle is mounted on an X-Y-Z manipulator stage to adjust the position of the nozzle with respect to the skimmer. Nozzle-skimmer distance is adjustable from 0 to 50 mm. Stagnation pressure in the nozzle is controlled by a commercial gas regulator from 1 to 100 atm. A He–Ne laser used for the adjustment of the beam alignment is mounted directly at the back of the nozzle (Fig. 1a) with 5-axis manipulator stages (X-, Y- and Z-stages and 2 tilt stages). Nozzle temperature for the He beam is controlled continuously from 60 to 500 K by a closed-cycle helium refrigerator (Fig. 1b) and a resistive heater (Fig. 1c) within a temperature fluctuation of ±0.1 K. For the molecular beam, temperature is controlled continuously only by the resistive heater from 300 to 900 K with the same resolution. Nozzle temperature is monitored by a type K (chromel/alumel) thermocouple spot-welded at the edge of the nozzle near the pinhole. The entire beam source unit (nozzle, manipulator, refrigerator and temperature control unit) is mounted on a square flange, as shown in Figure 1, for easy disassembly and maintenance.

Chamber 2 consists of a rotating disk chopper and a collimator. It is evacuated by a turbo-molecular pump with a pumping speed of 1500 l/s (for N_2). The BeCu chopper disk has four slots with two stage slits having widths of 0.7° and 45°. Chopper rotating frequency is controlled from 0 to 150 Hz which leads to a beam frequency of 0 to 600 Hz. The chopper unit is mounted on a movable stage for easy selection of continuous or pulsed operation by only adjusting one of the two slit widths as shown in Figure 1d. Chopper position can be monitored from the top view port. The temperature of the chopper motor is maintained below room temperature by a cold water flow placed in contact with the motor through stainless-steel tube. The temperature of the motor is monitored by a type K thermocouple attached to the motor.

Chamber 3 is evacuated by a tandem-type turbomolecular pump unit with pumping speeds of 520 and 250 l/s (for N_2), an ion pump with a pumping speed of 300 l/s (for N_2), and a titanium sublimation pump. The chamber is equipped with a 6-axis manipulator used for sample alignment (Fig. 1f) for molecular beam scattering or diffraction measurements. Sample position, crystal axis orientation, and tilt angle are set by the manipulator. The stages of the manipulator are mounted on a differentially pumped rotatable platform so that the incident and reflected angles of the molecular beam can be rotated without disturbing the alignment of the sample. Polar angle is varied by a stepper motor under computer control. The sample holder made of oxygen-free high-conductivity copper is attached to a liquid-nitrogen (LN_2) tank rod connected to the top flange of the manipulator. The sample is clamped by tantalum clips to obtain a good thermal contact with the sample holder. Sample temperature is maintained in the 91–1500 K range by electron bombardment heating and LN_2 cooling at a resolution of ±0.1°. Sample temperature is measured by a type K and/or a type C (W5%Re–W26%Re) thermocouple attached (or spot welded) to the edge of a sample. A homemade ion gun, a low energy electron diffraction and Auger electron spectroscopy (LEED/AES) system and a RAIRS system are also equipped in this chamber at the port shown in Figures 1e, 1g and 1i, and their bottom ports.

Chamber 4 provides a stage for differential pumping before the molecular beam enter the detector chamber. The chamber is evacuated by a tandem-type turbomolecular pump with pumping speeds of 550 l/s and 250 l/s (for N_2). Scattered molecules from chamber 3 pass through two apertures in chamber 4 before entering chamber 5.

Chamber 5 is evacuated by a tandem-type turbomolecular pump with pumping speeds of 600 l/s and 250 l/s (for N_2). It consists of a quadrupole mass spectrometer (ULVAC MSQ-400) and a tilt stage as shown in Figure 1j.

The detector units of chambers 4 and 5 can be attached at the port downstream of the molecular beam shown in Figure 1h for the time-of-flight measurements of the incident molecular beam.

2.2 Method

The distribution of incident translational energy is measured by a time-of-flight (TOF) technique. In conducting TOF measurement, the molecular beam is modulated in time using a mechanical chopper placed in chamber 2. The chopper with four slits of equal width is rotated at 150 Hz, where a time resolution of 13 μs is obtained. The signal is recorded by a multichannel analyzer with 2100 channels with 1 μs resolution. The start signal for the measurement is provided by a photocoupler, which is triggered by the moving slit of the chopper. All the measured TOF distributions are fitted with a Shifted-Maxwell-Boltzmann distribution, except for the low-energy He beam spectra. The measured TOF signal $h(t)$ is explicitly expressed as

$$h(t) = \int_{-\infty}^{\infty} s(t-\lambda) f(\lambda) d\lambda, \qquad (1)$$

where

$$f(t)dt = at^{-4} \exp\left(-\frac{m(l/t - v_d)^2}{2k_B T_g}\right) dt.$$

Also, $s(t)$ is the gate function for beam modulation which is described in Appendix A.1, t the flight time, l the flight path length of 838.5 mm, m the mass of the incident molecule and k_B the Boltzmann constant; a (intensity), v_d (drift speed) and T_g (beam temperature) are the parameters for analytical fitting. In all TOF measurements, uncertainty in time due to the experimental set-up [33] is properly corrected as described in Appendix A.2.

The angular intensity distribution measurement is carried out for scattered molecules from the surface by rotating the sample along the axis perpendicular to the beam line with an accuracy of ±0.1°. Throughout the present work, both incident and scattering angles are defined with respect to the surface normal direction. The sum of incident and scattering angles has been fixed at 90°. The angular intensity distribution obtained using a similar experimental apparatus and the same method [13, 34–36] has been used for verifying recent theoretical calculations [26–28], although the geometrical constraint causes the change in the incident angle in the measurement.

2.3 Fundamental properties of beam

2.3.1 He beam

The incident translational energy of He is controlled by regulating the nozzle temperature T_n and is determined by the time-of-flight measurement. The normalized time-of-flight spectra of low-energy He with a purity of >99.99995% are shown in Figure 2. Under our experimental condition, the intensity of the beam depends on nozzle-skimmer distance, the nozzle pinhole diameter N_ϕ, and stagnation pressure inside the nozzle P_0 as reported previously [33], while the shape of the time-of-flight spectra is found to be completely independent of nozzle-skimmer distance. Nozzle-skimmer distance in the experiment is, therefore, selected as the position for obtaining the highest beam intensity at the detector. The derived properties of the beam, the translational energy E_i of He estimated from the most probable velocity (drift speed) v_d, the corresponding wavelength λ, the energy spread $\Delta E/E$ and the Mach number M are shown in Table 1 together with T_n. Although not shown here, E_i is found to be independent of P_0, while $\Delta E/E$ decreases with an increase in P_0 as reported [33]. The coherent length ω of the He beam can be estimated from $\Delta E/E$, the wavelength λ of He and the geometrical conditions of the apparatus [31,37–39]. The estimated ω under our experimental set-up is about 16 nm,

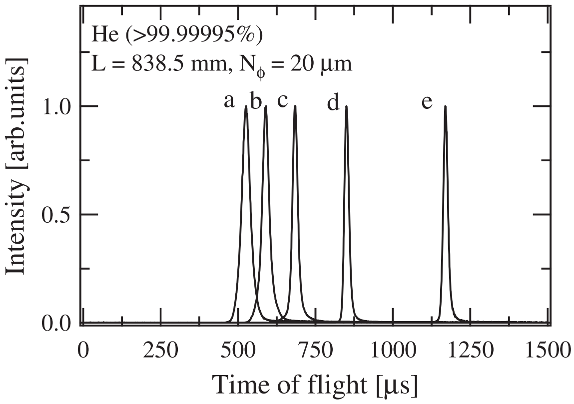

Fig. 2. Time-of-flight distributions of incident He. The flight pass length L and the nozzle pinhole diameter N_ϕ are 838.5 mm and 20 μm, respectively. The incident translational energies E_i derived from the spectra are a: $E_i = 53$, b: $E_i = 42$, c: $E_i = 31$, d: $E_i = 20$ and e: $E_i = 11$ meV. The beam properties are summarized in Table 1.

Table 1. Characteristics of low-energy incident He beams. The nozzle temperature T_n, most probable velocity of the beam (drift speed) v_d, incident translational energy E_i, wavelength λ, $\Delta E/E$ and Mach number M are listed.

T_n [K]	v_d [m/s]	E_i [meV]	λ[nm]	$\Delta E/E$ [%]	M
60	717	11	0.14	2.4	151
100	986	20	0.10	3.8	95
150	1226	31	0.081	5.7	63
200	1420	42	0.079	8.4	43
250	1594	53	0.062	11.8	31

which indicates that the apparatus is capable of providing structural information from the atomic scale to the dimensions of self-assembled nanostructures without any destruction by measurement using low-energy He atoms.

2.4 Supersonic molecular beams

The typical time-of-flight spectra of the Ar, CO and N_2 seeded in He are shown in Figure 3. The analytically fitted curves are also shown in the figure. In the present study, the molecular beam flux of Ar, CO and N_2 was kept at $(3.7 \pm 0.2) \times 10^{15}$ molecules/(cm^{2}s) by adjusting stagnation pressure [40]. In each case, the peak position is shifted to faster in TOF with increasing T_n. The most probable energy (incident kinetic energy) E_i and the beam temperature T_g derived from Figure 3 are plotted as functions of nozzle temperature in Figures 4a and 4b, respectively. In all cases, E_i and T_g increase with nozzle temperature T_n. The results of the calculation using

$$E_i|_{T_g}^{T_n} = \left(\frac{m_a \sum_j X_j}{\sum_j m_j X_j}\right) \int_{T_g}^{T_n} \frac{\left(\sum_j X_j C_{pj}\right)}{\left(\sum_j X_j\right)} dT \qquad (2)$$

are also shown in Figure 4a, where X_j is the mixing ratio of particle j, m the mass of the gas, a the target particle,

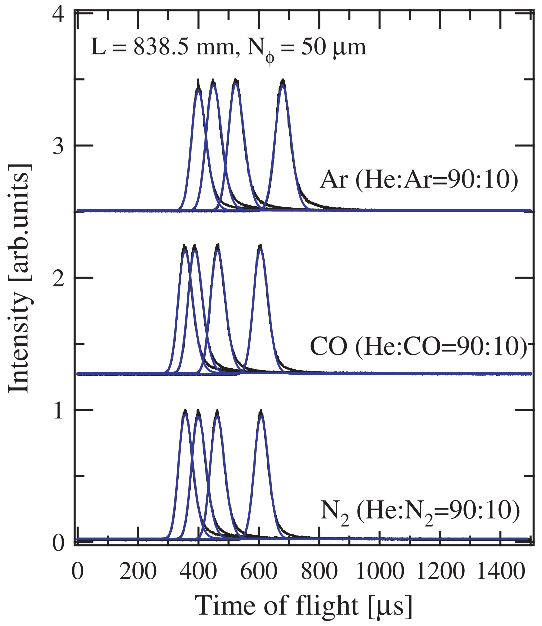

Fig. 3. Typical incident beam time-of-flight distributions of Ar, CO and N_2. The nozzle temperatures from right to left are $T_n = 300$, 500, 700 and 900 K. The corresponding incident translational energies derived from the spectra are described in Table 2.

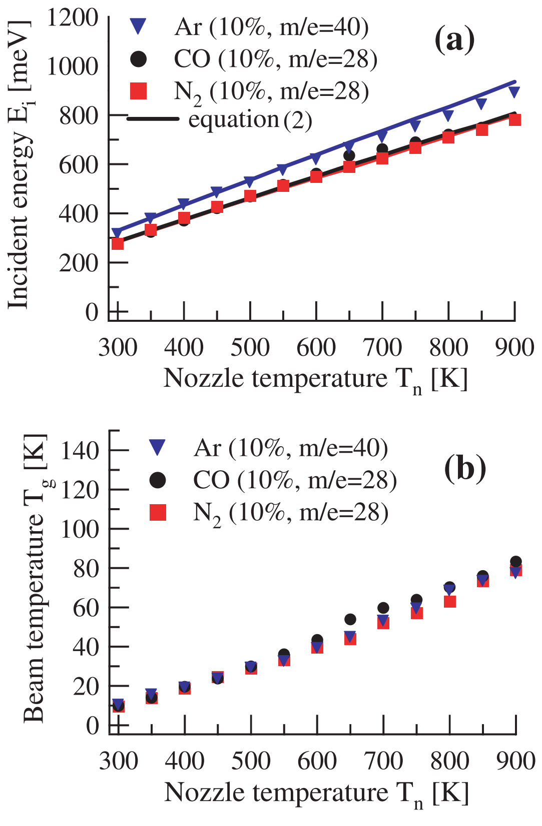

Fig. 4. (a) Incident kinetic energy E_i, (b) beam temperature T_g. Incident translational energies and beam temperatures of Ar, CO and N_2 derived from measured time-of-flight spectra.

Table 2. Characteristics of incident Ar, CO and N_2 beams. The nozzle temperature T_n, most probable velocity of the beam (drift speed) v_d, gas temperature T_g, incident translational energy E_i, $\Delta E/E$ and hydrodynamic speed ratio S are listed.

	T_n [K]	v_d [m/s]	T_g [K]	E_i [meV]	$\Delta E/E$ [%]	S
Ar	300	1228	10.3	314	17.7	18.9
	500	1585	29.1	524	23.1	14.4
	700	1841	53.0	707	26.9	12.4
	900	2065	77.2	890	28.8	11.6
CO	300	1377	9.85	277	18.6	18.1
	500	1790	29.6	469	25.2	13.5
	700	2126	59.7	661	29.6	11.3
	900	2315	83.3	783	32.2	10.4
N_2	300	1371	9.4	275	18.5	18.4
	500	1796	28.9	471	24.7	13.8
	700	2067	51.9	625	28.6	11.8
	900	2312	78.9	781	31.2	10.7

T_n the nozzle temperature and T_g the beam temperature. The isobaric specific heats C_p of Ar, CO, N_2 and He (gas for seeding) are assumed to be $(5/2)k_b$, $(7/2)k_b$, $(7/2)k_b$ and $(5/2)k_b$, respectively [41], at which we neglect the temperature dependence of C_p. Note that the equation (2) includes the beam temperature T_g which is derived from the analysis of the experimentally obtained time-of-flight spectra. Although in the case of ideal expansion (i.e. $T_g = 0$) the calculated results slightly deviate from the experimental results in Figure 4, the deviations become small by using experimentally obtained T_g in equation (2) as shown by the lines in Figure 4. The derived drift speed v_d, beam temperature T_g, incident translational energy E_i, $\Delta E/E$ and hydrodynamic speed ratio S are listed in Table 2 together with the nozzle temperature T_n (only typical conditions are listed). From the values in the table, it is confirmed that beam property significantly depends on T_n but not on the type of gas species.

2.5 Sample preparation

A LiF(001) sample 10×10 mm^2 was cleaved in air from a single crystalline rod and placed in the vacuum chamber in 10 min. The cleavage in air results in a clean and atomically flat surface with large terraces [42–45] so that scattering experiments could be performed immediately without any further treatment. The annealing of the crystal in ultrahigh vacuum (UHV) reduces the number of active sites for water adsorption [46,47] which takes place only when the crystal is cooled below 200 K [46]. The crystal used in this work was annealed several hours at 650 K in UHV. Surface cleanliness was confirmed from the sharp diffraction profile of He. He atom diffraction measurement was also employed to determine the incident azimuthal directions, namely [100] and [110].

Under our experimental conditions, no morphological change was confirmed from the He diffraction profiles of the LiF(001) surface after the irradiation of CO, N_2 and Ar, as in the case of irradiation of alkane molecules [34].

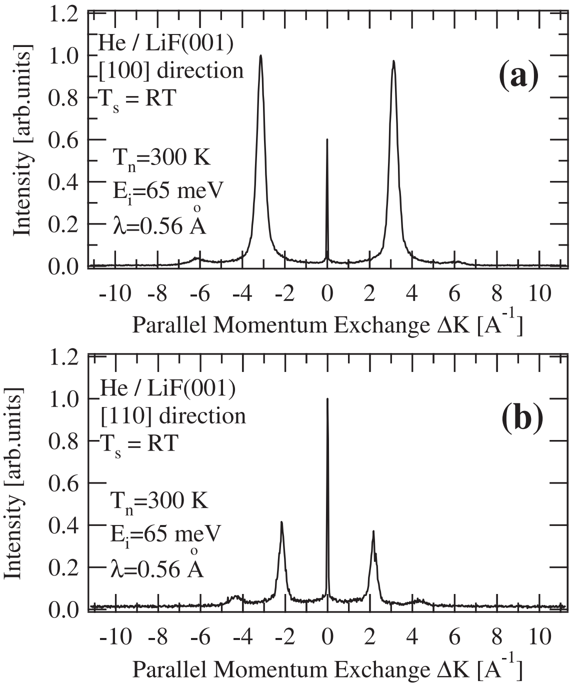

Fig. 5. He diffraction profiles of LiF(001). (a) Along the [100] azimuthal direction, (b) along the [110] azimuthal direction. The experimental conditions are shown in the figure.

3 Results and discussion

3.1 Diffractive scattering of He from LiF(001)

The angular intensity distributions of He scattered from LiF(001) along the [100] and [110] azimuthal directions are shown in Figures 5a and 5b, respectively. The k-vector of the abscissa axis corresponds to the obtained scattering angle of $0° \leq \theta \leq 90°$. Since the incident energy of the He beam is sufficiently small of 63 meV, the elastic scattering dominates in the distribution and the diffractive scattering can be observed as shown in Figure 5. The width of the specular peak is smaller than 0.5°, which is corresponding to the angular spread estimated from the geometrical condition of the apparatus shown in Figure 1. From the wavelength of the incident He beam and the peak position angles of the diffraction intensity profile, the lattice constant of the LiF(001) surface is derived as 4.02 ± 0.1, which corresponds to the recent high-precision measurement [48] of the LiF(001) lattice constant at a surface temperature of 300 K. The first-order diffraction peaks from the [100] direction are larger than the zero-order diffraction peak, indicating the large corrugation amplitude of the potential energy surface (PES) between He and LiF(001). From the comparison of the intensity difference among the diffraction peaks, the corrugation amplitude is confirmed to be larger for [100] than for [110], as has been previously reported in the literature [49,50].

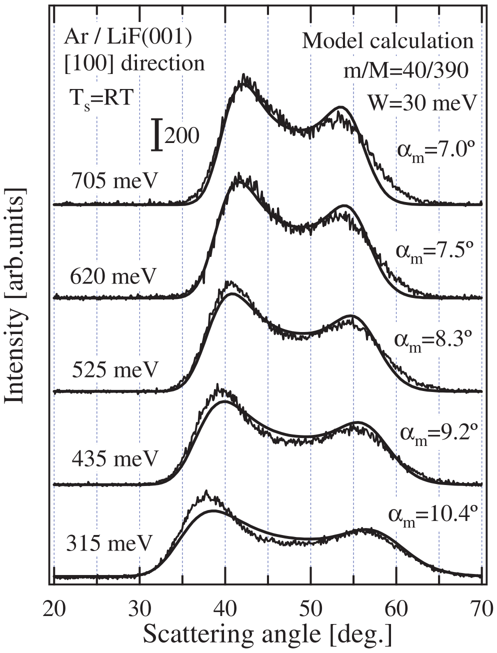

Fig. 6. Incident translational-energy dependences of angular intensity distributions of Ar. The experimental conditions are shown in the figure.

3.2 Rainbow scattering of Ar from LiF(001)

Figure 6 shows the angular intensity distributions of Ar scattered from LiF(001) along the [100] direction as a function of incident kinetic energy E_i. In every case, the rainbow feature of two intensity maxima due to the surface structural corrugation [8] is observed. The broadening of the angular intensity distribution is governed not only by surface structural corrugation but also by the relative motion of surface atoms with respect to the translational motion of incoming molecules. Thus, each peak becomes sharp with the increase in E_i as a result of the suppression of the relative surface atom motion. Apart from the relative surface atom motion, with increasing E_i, the two peaks come closer merging into a single peak and the total width of the distribution decreases as shown in Figure 6. This suggests that the corrugation amplitude of the apparent potential energy surface decreases with increasing E_i. The washboard model [9] analysis for Ar has also quantitatively indicated this feature, as shown by the lines in Figure 6, where the derived corrugation strength parameter α_m decreases with increasing E_i. This counterintuitive lessening of corrugation has also been observed for CH_4 and C_2H_6 scatterings [13,14,34,51] and has been attributed to a potential surface arising from two substrate ions of very different sizes [13,34].

From the washboard model analysis shown in Figure 6, another important parameter of the surface effective mass M was also derived as 390 amu. The surface effective mass is larger than the mass of LiF as conventionally determined in several scattering experiments using theoretical model analysis [4,10,13–15,26–29,32,34,52–57]. This has been attributed to the strong binding force among surface atoms that move as a whole [58].

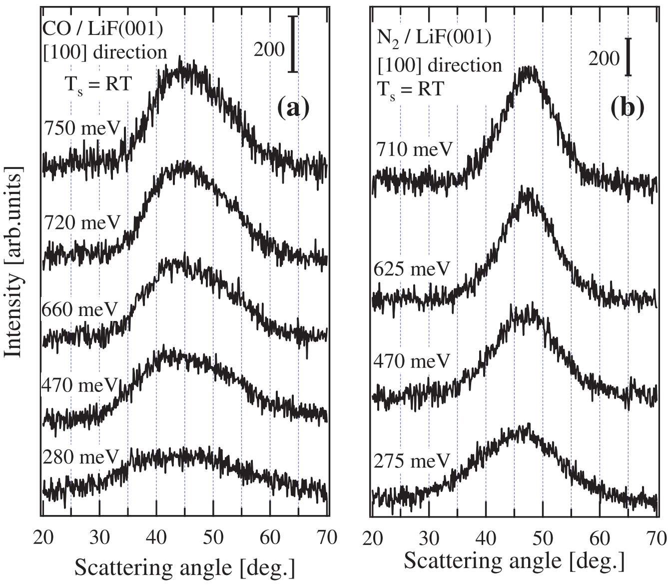

Fig. 7. Incident translational-energy dependences of angular intensity distributions of (a) CO and (b) N_2.

3.3 Effect of the molecular structural anisotropy

The angular intensity distributions of CO and N_2 scattered from LiF(001) along the [100] direction are shown in Figures 7a and 7b, respectively, as a function of incident kinetic energy E_i. Contrary to the case of atoms or spherical molecules, linear molecules such as CO and N_2 have a moment of inertia, causing translational-rotational energy transfer during collision. Therefore the scattering pattern becomes less sharp as can be seen in the comparison of Figure 7 with the Ar scattering shown in Figure 6 due to the increase in the inelastic collision event such as rotational mode excitation as a result of anti-symmetric molecular structure.

By applying the recently developed ellipsoid-washboard model [29], this feature can qualitatively be confirmed with its origin. The ellipsoid-washboard model treats the gas-surface scattering event as a single-collision event in the plane of incidence between the hard ellipsoid with mass m, ellipticity e and asymmetric parameter ε, and the surface cube of the hard repulsive wall with effective mass M. As the main assumption of the model, the tangential momentum with respect to the surface cube (local tangential momentum) of the molecule colliding with the surface is conserved as in the case of conventional cube models [7,59–61]. However the surface cube locates sinusoidally on the surface with corrugation strength α_m as like a washboard model [9]. Thus the global tangential momentum of the molecule is not conserved. If the molecular structural anisotropy (ellipticity e of the incident hard ellipsoid) is selected as 1.0 (i.e. the molecule becomes the point with mass)

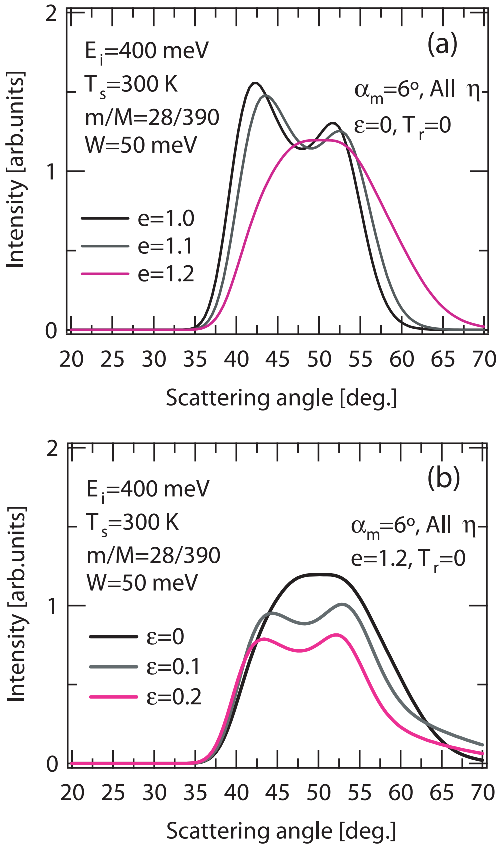

Fig. 8. Calculated results [62] based on the ellipsoid-washboard model. (a) Dependence on the molecular structural anisotropy e, (b) dependence on the center-of-mass position (asymmetric parameter ε).

and the corrugation strength α_m is selected as 0 (i.e. the surface is flat), the model becomes the same as the original hard-cube model. When the ellipticity e increases, the peak positions of the rainbow feature due to the surface structural corrugation approach each other as shown by the calculated results [62] based on the ellipsoid-washboard model [29] in Figure 8a, which indicates smearing of the apparent surface corrugation (disappearance of the rainbow feature).

The smearing effect is caused by the strong dependence of the angular intensity distribution on the molecular orientation at the collision. For collisions occurring "end-on" or "side-on", there is no torque on the molecule during collision and, hence, no rotational mode excitation occurs. The angular intensity distribution in this initial molecular orientation then becomes the same with that for atoms. On the other hand, for collisions occurring at the intermediate orientation angles, there is a large torque during collision and then the rotational mode excitation takes place. In this case, the peak position of the angular intensity distribution shifts towards large scattering angle due to the energy exchange from normal component of the incident translational energy to the rotational mode excitation as well as the phonon creation on the surface based on the model calculations [29]. Since the experimentally obtained angular distribution corresponds to the summation of these every initial orientation case, rainbow scattering is smeared out by this summation even on the structurally corrugated surface due to the molecular structural anisotropy as shown in Figure 8a.

The rainbow scattering as like Ar scattering in Figure 6 is therefore considered to be not observable for the N_2 scattering distribution from a corrugated LiF surface, as shown in Figure 7a. The same tendency was also observed [14,34,64] in the angular intensity distribution of C_2H_6 from LiF(001), though rainbow scattering in the mean energy angular distribution is not completely smeared out [64]. The difference in the angular intensity distributions between that of CO and N_2 will be discussed below.

3.4 Effect of the center-of-mass position

In contrast to the case of N_2 scattering, the CO molecule shows a rainbow feature in the scattering pattern as shown in Figure 7b though it has the same molecular mass and linear structure as those of the N_2 molecule. The difference is considered to be due to the deviation of the center-of-mass position of CO from the molecular center.

When the center-of-mass shifts from the molecular center, the collision dynamics separates in two types depending on the initial molecular orientation angle, i.e. large-mass-end and small-mass-end cases. In the large-mass-end case, the molecule behaves like a heavy sphere resulting in scattering with a weak orientation dependence of intensity distribution and a slight translational-rotational energy transfer, while the molecule behaves like a long ellipsoid resulting in trapping and/or multiple collision induced by the translational-rotational energy transfer due to the large moment of inertia in the small-mass-end case. Summation of the angular intensity distributions in every orientation case, therefore, becomes similar to the distribution of the large-mass-end case because the scattered intensity for the small-mass-end case becomes weak as a result of trapping and/or the multiple collision. Therefore, as shown in Figure 7, the rainbow scattering of CO is not completely smeared out in contrast to the case of N_2.

The effect of the center-of-mass position on the scatterings from corrugated surfaces mentioned above can be qualitatively confirmed by the calculated results based on the ellipsoid washboard model [29] in Figure 8b. When the asymmetry parameter ε increases, the total scattered intensity becomes small due to the increasing of the events of trapping and/or the multiple collision for the small-mass-end case and the rainbow feature in the large-mass-end case is observed without smearing as like CO scattering case in Figure 7b. This tendency also agrees with the reported experimental results of "rotational trapping" in the CO scattering from Ni(111), i.e., the scattered intensity of the O-end collision of CO is larger than that of C-end collision due to the more extensive translational-rotational energy-transfer process for C-end collision [18]. The same tendency can also be seen in the reported NO scattering from Pt(111) (Ref. [65]) and Ni(110) (Ref. [66]). In both cases, the sticking probability of the N-end collision of NO is reported to be larger than that of O-end collision. Consequently, the total scattered intensity from the surface decreases and the distribution width of the main peak becomes narrower with increasing asymmetry parameter, as shown in Figure 8b. This tendency of the angular intensity distribution can be identified in the experimental diatomic and polyatomic molecules scattering from flat Ag(111) surface as reported in the literature [67].

The effect of the center-of-mass position on the gas-surface interaction can also be seen in the literatures in the experimental works dealing with the effect of the molecular orientation on the gas-surface interaction at the flat surface. Most of such experimental results were well reproduced by the molecular dynamics simulations using both the attractive and the repulsive potential with strong anisotropy depending on the orientation of the molecule between NO and the surface [11,19,68]. Contrary to the case of such detailed treatments, several untreated factors are remained in the simple ellipsoid-washboard model. However, it gives us a conceptual agreement with angular intensity distributions of Ar, CO and N_2 from LiF(001) experimentally obtained such that the difference in the rainbow feature was reproduced as discussed above. To fully understand the effect of molecular structure on the gas-surface scattering, it would be useful to compare our presented results with the calculated results under different theory [23,24], or with the results of the trajectory simulations [11,19,68,69] by utilizing accurate potential energy surfaces as well as obtaining the another experimental results as a future work.

4 Summary

We have newly developed experimental apparatus for investigating the gas-surface interaction. By the measurements of the time-of-flight of He beam and of the angular intensity distributions of He scattered from LiF(001), the coherent length of the helium, the energy resolution and the angular spread of the beam in the apparatus were established as $\omega = 16$ nm, $\Delta E/E = 2.4\%$ and $\Delta\theta = 0.5°$, respectively.

The diffractive scattering of He and the rainbow scattering of Ar, CO and N_2 have been measured by the angle-resolved intensity measurement from LiF(001) along the [100] azimuthal direction as a function of incident translational energy. The effects of the molecular structure on the rainbow scattering were discussed in terms of the molecular structural anisotropy and center-of-mass position with predictions based on the recently developed simple classical theory of the ellipsoid-washboard model. Although several untreated factors are remained in the model, the simple ellipsoid-washboard model gives us a conceptual agreement with angular intensity distributions of Ar, CO and N_2 experimentally obtained such that the difference in the rainbow feature was reproduced.

We would like to express our gratitude to all the staff of the Surface Chemistry Laboratory in RIKEN for their fruitful discussions and continuous encouragement. We would also like to thank Mr. M. Saida and Miss S. Mae for adjusting the alignment of the molecular beam. We are grateful to Dr. T. Miyake (Hitachi Ltd) for providing us with original drawings of the supersonic molecular beam chamber and for advice on some aspects of the construction of the apparatus, and to staff of Vieetech Ltd. and Mr. K. Shirasaka for their help in setting up the apparatus. One of the authors (T.K.) appreciates the financial support from the SPR System in RIKEN.

Appendix A: Treatment of time-of-flight spectra

The detailed treatments of the time-of-flight spectra for the estimation of fundamental properties of the beam are described in this section.

A.1 Gate function

The gate function for the beam modulation $s(t)$ discussed in Section 2.2 is explicitly expressed as

$$0 \le t \le \frac{r}{v} \qquad s(t) = \frac{2}{\pi r^2}\left\{\frac{\pi r^2}{2\pi}\cos^{-1}\frac{r-vt}{r} - \frac{(r-vt)^2}{2}\tan\left(\cos^{-1}\frac{r-vt}{r}\right)\right\}$$

$$\frac{r}{v} \le t \le 2\frac{r}{v} \qquad s(t) = \frac{1}{\pi r^2}\left[\pi r^2 - r^2\left(\pi - \cos^{-1}\frac{r-vt}{r}\right) + \left\{v\left(t-\frac{r}{v}\right)\right\}^2\tan\left(\pi-\cos^{-1}\frac{r-vt}{r}\right)\right]$$

$$2\frac{r}{v} \le t \le \frac{R}{v} \qquad s(t) = 1$$

$$\frac{R}{v} \le t \le \frac{R+r}{v}$$

$$s(t) = \frac{1}{\pi r^2}\left[\pi r^2 - r^2\cos^{-1}\left(1-\frac{vt-R}{r}\right) + \left\{r - v\left(t-\frac{R}{v}\right)\right\}^2\tan\left\{\cos^{-1}\left(1-\frac{vt-R}{r}\right)\right\}\right]$$

$$\frac{R+r}{v} \le t \le \frac{R+2r}{v}$$

$$s(t) = \frac{1}{\pi r^2}\left[r^2\left\{\pi - \cos^{-1}\left(1-\frac{vt-R}{r}\right)\right\} - (vt-R-r)^2\tan\left(\pi - \cos^{-1}\left(1-\frac{vt-R}{r}\right)\right)\right]$$

$$\frac{R+2r}{v} \le t \qquad s(t) = 0,$$

where r is the radius of the beam spot at the chopper, R the half length of the chopper gate, and v the angular velocity of the chopper. The density distribution of the beam in the spot at the chopper is assumed to be uniform.

A.2 Correction of time

The correction of uncertainty in time due to the experimental set-up [33] is described here. The main deviation of time originates from the "start signal" and the "detection time" as $\varDelta_{ta}$ and $\varDelta_{tb}$, respectively.

$\varDelta_{ta}$ is the difference between the "molecular beam start time" and the "trigger start time provided by the photocoupler". Since the photocoupler is located at the 45° rotated position from the beam modulation position in the chopper disk, the slight geometrical deviation results in the deviation of the start time signal of the beam modulation. To correct such a deviation, the time-of-flight spectra of the He beam under the same energy condition are measured at several chopper rotation speeds. The peak position difference of the spectra originates from the geometric deviation of the photocoupler from beam modulation, while the difference in width originates from the chopper gate function. From the difference in peak position, the geometrical deviation is estimated and $\varDelta_{ta}$ is corrected at a chopper rotation speed corresponding to that used in the measurement.

$\varDelta_{tb}$ is the time of flight of the molecule in the detector after the molecule was ionized at the top of quadrupole mass spectrometer shown in Figure 1f. After entering the ionization part, the ionized molecules fly a quadrupole distance of 200 mm with 13.1 V applied, taking about a few dozen microseconds depending on intended mass. $\varDelta_{tb}$ is corrected by subtracting time.

References

1. J.A. Barker, D.J. Auerbach, Surf. Sci. Rep. **4**, 1 (1985)
2. C.T. Rettner, M.N.R. Ashfold, *Dynamics of Gas-Surface Interactions* (The Royal Society of Chemistry, 1991)
3. R.J. Madix, *Surface Reactions* (Springer-Verlag, 1994)
4. C.T. Rettner, D.J. Auerbach, J.C. Tully, A.W. Kleyn, J. Phys. Chem. **100**, 13021 (1996)
5. M. Bonn, A.W. Kleyn, G.J. Kroes, Surf. Sci. **500**, 475 (2002)
6. A.W. Kleyn, Chem. Soc. Rev. **32**, 87 (2003)
7. R.M. Logan, R.E. Stickney, J. Chem. Phys. **44**, 195 (1966)
8. A.W. Kleyn, T.C.M. Horn, Phys. Rep. **199**, 191 (1991)
9. J.C. Tully, J. Chem. Phys. **92**, 680 (1990)
10. B. Berenbak, S. Zboray, B. Riedmuller, D.C. Papageorgopoulos, S. Stolteb, A.W. Kleyn, Phys. Chem. Chem. Phys. **4**, 68 (2002)
11. R.J. Lahaye, S. Stolte, S. Holloway, A.W.Kleyn, J. Chem. Phys. **104**, 8301 (1996)
12. J.A. Stinett, R.J. Madix, J.C. Tully, J. Chem. Phys. **104**, 3134 (1996)
13. T. Tomii, T. Kondo, S. Yagyu, S. Yamamoto, J. Vac. Sci. Technol. A **19**, 675 (2001)
14. T. Kondo, T. Tomii, S. Yagyu, S. Yamamoto, J. Vac. Sci. Technol. A **19**, 2468 (2001)
15. T. Kondo, D. Mori, R. Okada, M. Sasaki, S. Yamamoto, J. Chem. Phys. **123**, 114712 (2005)
16. A.W. Kleyn, A.C. Luntz, D.J. Auerbach, Phys. Rev. Lett. **47**, 1169 (1981)
17. K.R. Lykke, B.D. Kay, J. Phys. Condens. Matter **3**, S65 (1991)
18. M.A. Hines, R.N. Zare, J. Chem. Phys. **98**, 9134 (1993)
19. A.W. Kleyn, Prog. Surf. Sci. **54**, 407 (1997)
20. J.C. Polanyi, R.J. Wolf, J. Chem. Phys. **82**, 1555 (1985)
21. D.C. Jacobs, R.N. Zare, J. Chem. Phys. **91**, 3196 (1989)
22. J. Harris, A.C. Luntz, J. Chem. Phys. **91**, 6421 (1989)
23. I. Iftimia, J.R. Manson, Phys. Rev. Lett. **87**, 093201 (2001)
24. I. Iftimia, J.R. Manson, Phys. Rev. B **65**, 125401 (2002)
25. I. Iftimia, J.R. Manson, Phys. Rev. B **65**, 125412 (2002)
26. I. Moroz, J.R. Manson, Phys. Rev. B **69**, 205406 (2004)
27. I. Moroz, H. Ambaya, J.R. Manson, J. Phys. Condens. Matter **16**, S2953 (2004)
28. I. Moroz, J.R. Manson, Phys. Rev. B **71**, 113405 (2005)
29. T. Kondo, H.S. Kato, T. Yamada, S. Yamamoto, M. Kawai, J. Chem. Phys. **122**, 244713 (2005)
30. F. Murakami, S. Yagyu, E.S. Gillman, M. Mizunuma, Y. Takeishi, Y. Kino, H. Kita, S. Yamamoto, J. Surf. Anal. **3**, 481 (1997)
31. T. Kondo, Ph.D. thesis, University of Tsukuba, 2003
32. T. Kondo, D. Mori, R. Okada, S. Yamamoto, Jpn J. Appl. Phys. **43**, 1104 (2004)
33. G. Scoles, *Atomic and Molecular Beam Methods* (Oxford University Press, New York, 1988), Vol. 1; (1992), Vol. 2
34. T. Kondo, T. Tomii, T. Hiraoka, T. Ikeuchi, S. Yagyu, S. Yamamoto, J. Chem. Phys. **112**, 9940 (2000)
35. T. Kondo, T. Sasaki, S. Yamamoto, J. Chem. Phys. **116**, 7673 (2002)
36. T. Kondo, T. Sasaki, S. Yamamoto, J. Chem. Phys. **118**, 760 (2003)
37. G. Comsa, Surf. Sci. **81**, 57 (1979)
38. D. R. Frankl, Surf. Sci. **84**, L485 (1979)
39. G. Comsa, Surf. Sci. **84**, L489 (1979)
40. The beam flux is estimated by $Q_a = \frac{P_1-(\chi_a+\chi_b)P_0}{(\chi_a/S_a)+(\chi_b/S_b)X_b}\frac{1}{(\pi r^2)}$ [Torr l/(cm^{2}s)], where P_1, P_0 is the pressure in the chamber 3 (beam on and off, respectively) measured by the ion gauge, S_j the pumping speed for the particle j in the chamber 3, χ_j the ionization probability for particle j, X_b the amount ratio of the particle b against particle a in the mixed beam and r the radii of the beam spot at the sample ($r = 0.25/2$ cm)
41. P.W. Atkins, *Physical Chemistry*, 6th edn. (Oxford University Press, 1998)
42. M.J. Yacaman, Z.T. Ocana, J. Appl. Phys. **48**, 418 (1977)
43. H. Höche, H. Bethge, J. Cryst. Growth. **33**, 246 (1976)
44. G. Meyer, N.M. Amer, J. Appl. Phys. **56**, 2100 (1990)
45. G. Lange, J.P. Toennies, R. Vollmer, H. Weiss, J. Chem. Phys. **98**, 10096 (1993)
46. P. Barraclough, P.G. Hall, Surf. Sci. **46**, 393 (1974)
47. J. Estel, H. Hoinkes, H. Kaarman, H. Nahr, H. Wilsch, Surf. Sci. **54**, 393 (1976)
48. Y. Ekinci, J.P. Toennies, Surf. Sci. **563**, 127 (2004)
49. N. Garcia, J. Chem. Phys. **67**, 897 (1977)
50. H. Legge, J.R. Manson, J.P. Toennies, J. Chem. Phys. **110**, 8767 (1999)
51. T. Tomii, T. Kondo, T. Hiraoka, T. Ikeuchi, S. Yagyu, S. Yamamoto, J. Chem. Phys. **112**, 9052 (2000)
52. S. Yagyu, F. Murakami, Y. Kino, S. Yamamoto, Jpn J. Appl. Phys. **37**, 2642 (1998)
53. A.C. Wight, R.E. Miller, J. Chem. Phys. **109**, 1976 (1998)
54. G. Armand, J. Lapujoulade, Y. Lejay, Surf. Sci. **63**, 143 (1977)

55. C. R. Arumainayagam, M.C. McMaster, G.R. Schoofs, R.J. Madix, Surf. Sci. **222**, 213 (1989)
56. D. Velic, R.J. Levis, Chem. Phys. Lett. **269**, 59 (1997)
57. T. Kondo, R. Okada, D. Mori, S. Yamamoto, Surf. Sci. **566-568**, 1153(2004)
58. E.K. Grimmelmann, J.C. Tully, M.J. Cardillo, J. Chem. Phys. **72**, 1039 (1980)
59. W.L. Nichols, J.H. Weare, J. Chem. Phys. **62**, 3754 (1975)
60. W.L. Nichols, J.H. Weare, J. Chem. Phys. **63**, 379 (1975)
61. W.L. Nichols, J.H. Weare, J. Chem. Phys. **66**, 1075 (1977)
62. In the calculation, the rotational temperature of the molecule T_r is set to as 0 K, since T_r of the supersonic molecular beam is generally cold enough to neglect the effect on the intensity distribution. The probability $S(\eta, \omega/V_r)$ of a collision is assumed to be uniform, occurring at all molecular orientation angles η, since it has almost the same probabilities for all cases under our experimental conditions. The molecular mass is set to as 28 amu of CO and N_2. The effective mass of the surface is set to 390 amu, which is derived from the analysis of the experimental Ar–LiF(001) scattering as shown in Figure 6 and as described the origin in Section 3.2. The moment of inertia is derived by the simple calculation of $\frac{m_a \times m_b}{m_a + m_b} r_d^2$, where r_d is selected as reported value of CO ($r_d = 0.1128$ nm) from the hand book [63]. The semi-major axis of the ellipsoid b is set to 0.15 nm. Our experimental condition of $\theta + \theta' = 90^\circ$ is included in the calculation for easy comparison with our experimental results.
63. D.R. Lide, *CRC Handbook of Chemistry and Physics*, 81th edn. (CRC, New York, 1998), pp. 9-82
64. T. Kondo, T. Tomii, S. Yamamoto, Chem. Phys. (2005) in press
65. E.W. Kuipers, M.G. Tenner, A.W. Kleyn, S. Stolte, Phys. Rev. Lett. **62**, 2152 (1989)
66. G.H. Fecher, N. Bowering, M. Volkmer, B. Pawlitzky, U. Heinzmann, Surf. Sci. **230**, L169 (1990)
67. H. Asada, Jpn J. Appl. Phys. **20**, 527 (1981)
68. M.G. Tenner, E.W. Kuipers, A.W. Kleyn, Surf. Sci. **242**, 376 (1991)
69. For example. C.T. Reeves, B.A. Ferguson, C.B. Mullins, G.O. Sitz, B.A. Helmer, D.B. Graves, J. Chem. Phys. **111**, 7567 (1999)